Altered action potential waveform and shorter axonal initial segment in hiPSC-derived motor neurons with mutations in VRK1

Rémi Bos, Khalil Rihan, Patrice Quintana, Lara El-Bazzal, Nathalie Bernard-Marissal, Nathalie da Silva, Rosette Jabbour, André Mégarbané, Marc Bartoli, Frédéric Brocard, et al.

▶ **To cite this version:**

Rémi Bos, Khalil Rihan, Patrice Quintana, Lara El-Bazzal, Nathalie Bernard-Marissal, et al.. Altered action potential waveform and shorter axonal initial segment in hiPSC-derived motor neurons with mutations in VRK1. Neurobiology of Disease, 2022, 164, pp.105609. 10.1016/j.nbd.2021.105609 . hal-04323628

HAL Id: hal-04323628

https://amu.hal.science/hal-04323628v1

Submitted on 20 Nov 2024

HAL is a multi-disciplinary open access archive for the deposit and dissemination of scientific research documents, whether they are published or not. The documents may come from teaching and research institutions in France or abroad, or from public or private research centers.

L'archive ouverte pluridisciplinaire **HAL**, est destinée au dépôt et à la diffusion de documents scientifiques de niveau recherche, publiés ou non, émanant des établissements d'enseignement et de recherche français ou étrangers, des laboratoires publics ou privés.

Distributed under a Creative Commons Attribution - NonCommercial - NoDerivatives 4.0 International License

Neurobiology of Disease 164 (2022) 105609

Contents lists available at ScienceDirect

Neurobiology of Disease

journal homepage: www.elsevier.com/locate/ynbdi

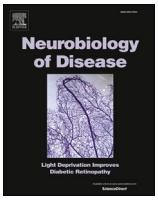

Altered action potential waveform and shorter axonal initial segment in hiPSC-derived motor neurons with mutations in *VRK1*

Rémi Bos [a,**,1], Khalil Rihan [b,1], Patrice Quintana [b], Lara El-Bazzal [b], Nathalie Bernard-Marissal [b], Nathalie Da Silva [b], Rosette Jabbour [c], André Mégarbané [d], Marc Bartoli [b], Frédéric Brocard [a,1], Valérie Delague [b,1,*]

[a] Aix Marseille Univ, CNRS, Institut de Neurosciences de la Timone (INT), UMR 7289, Marseille, France
[b] Aix Marseille Univ, Inserm, MMG, U 1251, Institut Marseille Maladies Rares (MarMaRa), Marseille, France
[c] Neurology Division, Department of Internal Medicine, St George Hospital University Medical Center, University of Balamand, Beirut, Lebanon
[d] Department of Human Genetics, Gilbert and RoseMary Chagoury Hospital, Lebanese American University, Byblos, Lebanon

ARTICLE INFO

Keywords:
Motoneuron
Action potential waveform
VRK1
hiPSC
Inherited peripheral neuropathy
Motor neuron disease
Axonal initial segment
Firing pattern

ABSTRACT

We recently described new pathogenic variants in *VRK1*, in patients affected with distal Hereditary Motor Neuropathy associated with upper motor neurons signs. Specifically, we provided evidences that hiPSC-derived Motor Neurons (hiPSC-MN) from these patients display Cajal Bodies (CBs) disassembly and defects in neurite outgrowth and branching. We here focused on the Axonal Initial Segment (AIS) and the related firing properties of hiPSC-MNs from these patients. We found that the patient's Action Potential (AP) was smaller in amplitude, larger in duration, and displayed a more depolarized threshold while the firing patterns were not altered. These alterations were accompanied by a decrease in the AIS length measured in patients' hiPSC-MNs. These data indicate that mutations in VRK1 impact the AP waveform and the AIS organization in MNs and may ultimately lead to the related motor neuron disease.

1. Introduction

Mutations in *VRK1* are responsible for a wide spectrum of neurological diseases such as spinal Muscular Atrophy (SMA), distal SMA (adult-onset), Amyotrophic Lateral Sclerosis (ALS), juvenile ALS, Hereditary Motor and Sensory Neuropathy (Charcot-Marie-Tooth disease) or pure motor neuropathy (distal Hereditary Motor Neuropathy (dHMN)) (Renbaum et al., 2009; El-Bazzal et al., 2019). In total, 20 mutations are now reported in *VRK1* in 30 patients from 18 families, affected with diseases described under several different clinical entities: Spinal Muscular Atrophy (SMA), distal SMA (adult-onset), Amyotrophic Lateral Sclerosis (ALS), juvenile ALS, Hereditary Motor and Sensory Neuropathy (Charcot-Marie-Tooth disease), pure motor neuropathy (distal Hereditary Motor Neuropathy (dHMN)). There is no clear phenotype-genotype correlation, but the common feature to all patients is the involvement of lower motor neurons (MNs). *VRK1* encodes an ubiquitously expressed, mainly nuclear, serine/threonine kinase, playing a crucial role in many cellular processes like cell division and cell cycle progression (Valbuena et al., 2008, 2011).

We recently identified two new mutations in *VRK1*, in two siblings from a Lebanese family, affected with dHMN associated with upper motor neurons (MNs) signs (El-Bazzal et al., 2019). By studying patient's cells, including induced Pluripotent Stem Cell (iPSC) derived Motor Neurons (hiPSC-MNs), we have shown that the mutations in *VRK1* reduced levels of VRK1 in the nucleus (El-Bazzal et al., 2019). This depletion alters the dynamics of coilin, a phosphorylation target of VRK1 (Sanz-Garcia et al., 2011; El-Bazzal et al., 2019). Coilin is the main component and scaffold protein of the Cajal Bodies (CBs) required for splicing, ribosome biogenesis and telomere maintenance (Lafarga et al., 2017). CBs are particularly prominent in post-mitotic neurons and

* Corresponding author at: Inserm U 1251, Marseille Medical Genetics, Faculté de Médecine de la Timone, Aix Marseille Université, 27 bd Jean Moulin, 13385 Marseille cedex 05, France.
** Corresponding author at: Institut de Neurosciences de la Timone, Centre National de la Recherche Scientifique (CNRS) and Aix-Marseille Université, UMR 7289, 27 bd Jean Moulin, 13385 Marseille cedex 05, France.
E-mail addresses: remi.bos@univ-amu.fr (R. Bos), valerie.delague@univ-amu.fr (V. Delague).
[1] These authors contributed equally.

https://doi.org/10.1016/j.nbd.2021.105609
Received 20 April 2021; Received in revised form 24 October 2021; Accepted 30 December 2021
Available online 3 January 2022
0969-9961/© 2022 The Authors. Published by Elsevier Inc. This is an open access article under the CC BY-NC-ND license (http://creativecommons.org/licenses/by-nc-nd/4.0/).

anomalies of CBs, such as the ones described by us in VRK1 patients' hiPSC-MNs (El-Bazzal et al., 2019), are also hallmarks of Spinal Muscular Atrophy (SMA), another MN disease (lower MN) caused by loss or mutations in the Survival Motor Neuron (SMN) protein (Tapia et al., 2012).

The use of human induced pluripotent stem cells (hiPSCs) (Takahashi et al., 2007; Takahashi and Yamanaka, 2006) represent a unique opportunity to study human neuronal and glial cells affected in motor neuron diseases and Inherited Peripheral Neuropathies, while maintaining the disease-associated genetic background of the patient (Saporta et al., 2011). One particular interest is the possibility to measure the electrical activity of these neurons, as demonstrated in a few studies in hiPSC-MNs from patients with Amyotrophic Lateral Sclerosis (ALS) (Sances et al., 2016; Toli et al., 2015; Wainger et al., 2014), Spinal Muscular Atrophy (SMA) (Liu et al., 2015) and Charcot-Marie-Tooth disease (CMT) (Saporta et al., 2015). In our previous work (El-Bazzal et al., 2019), we have demonstrated that hiPSC-MNs from patients with bi-allelic mutations in *VRK1* have shorter neurite length and altered branching, consistent with a length dependent axonopathy. However, putative structural changes of the axon initial segment (AIS), the site governing the spike initiation, remain unknown.

Here, we studied the electrophysiological properties of hiPSC-MNs from patients with mutations in *VRK1* as compared to controls. We confirmed that the used differentiation protocol induces functional hiPSC-MNs capable of displaying sustained firing patterns. We also demonstrated that co-culture with mouse myoblasts enhance the functional maturation of hiPSC-MNs. In hiPSC-MNs from patients with VRK1 mutations, the Action Potential (AP) was smaller in amplitude and larger in duration. This modification of AP appears to result from a decrease in the Axonal Initial Segment (AIS) length. These data indicate that mutations in VRK1 contribute to the alteration of the spiking features that may ultimately lead to the upper and lower motor neuron disease affecting these patients.

2. Material and methods

2.1. Patients' cells and cell lines

The control hiPSC cell line was provided by MaSC, our Cell Reprogramming and Differentiation Facility at U1251/Marseille Medical Genetics (Marseille, France). This hiPS cell line was obtained by reprogrammation of a commercial fibroblast cell line (FibroGRO™ Xeno-Free Human Foreskin Fibroblasts, #SCC058, Merck Millipore, Germany). The patient hiPSC cell line was obtained by reprogrammation of skin primary fibroblasts from the female patient II.2, affected with autosomal recessive distal Hereditary Motor Neuropathy (dHMN), due to bi-allelic in *VRK1* described in (El-Bazzal et al., 2019). All hiPSCs included in the study are declared in a collection authorized by the competent authorities in France (declaration number DC-2018-3207). The mouse C2C12 myoblast cell line (#ATCC CRL-1772) (Yaffe and Saxel, 1977) was obtained from ATCC-LGC Standards (USA).

2.2. Generation, culture and maintenance of hiPSCs

Reprogrammation of skin fibroblasts from patient and control into induced pluripotent stem cells (hiPSC) was performed by our Cell Reprogramming and Differentiation Facility (MaSC) at U 1251/Marseille Medical Genetics (Marseille, France), using Sendai virus-mediated transduction (Thermofisher Scientific, #A16517) or nucleofection (Amaxa, Lonza, # VAPD-1001 NHDF) of episomal vectors containing OCT3/4, SOX2, KLF4, C-MYC and shRNA against p53. hiPSCs colonies were picked about two weeks after transduction/nucleofection based on ES cell-like morphology. Colonies were grown and expanded in mTeSR1 medium (Stemcells technologies, #85850) on BD Matrigel™ (Corning, #354277) coated dishes. hiPSCs clones were fully characterized using classical protocols as described in (El-Bazzal et al., 2019).

After thawing, hiPSCs were plated on Matrigel (Corning Life Sciences, USA, #354248) coated plastic dishes and maintained in mTeSR1 medium (Stemcell Technologies, Canada, #05851), which was exchanged daily.

2.3. Differentiation of hiPSCs into spinal Motor Neurons (hiPSC-MNs)

For differentiation of hiPSCs into spinal MNs, we used an established 30 days differentiation protocol based on early activation of the Wnt signaling pathway, coupled to activation of the Hedgehog pathway and inhibition of Notch signaling (Maury et al., 2015).

Briefly, at Day 0, hiPSCs were dissociated with accutase (Thermofisher Scientific, # A11105–01), when 70–90% confluent, and cultured, in suspension, in non-adherent, ultra-low attachment, 10 cm Petri dishes to form Embryoide Bodies (EB) in "N2B27" medium supplemented with ROCK inhibitor Y-27632 (Selleckchem, #51049) at 10 μM, 20 μM of SB431542 (Stemgent, #04–0010), 0.1 μM LDN193189 (Stemgent, #04-0074), 3 μM CHIR-99021 (Selleck, #51263) and 10 μM Ascorbic Acid (AA) (Sigma, #A 0278-100G).The "N2B27" medium is composed of equal volumes of ADMEM/F12 (Thermofisher Scientific, # 12634-028) and Neurobasal-A medium (Thermofisher Scientific, #10888-022), supplemented with N2 supplement (Thermofisher Scientific, # 17502-048), B-27 Supplement minus vitamin A (Thermofisher Scientific, #12587010), 200 mM Glutamax (Thermo Fisher Scientific, #35050-038).), 0.2 mM 2-mercaptoethanol (Thermofisher Scientific, #31350-010) and Penicillin/Streptomycin 1% (Thermofisher Scientific, #15070063).

At Day 2, EBs were transferred to a new dish and cultured in N2B27 supplemented with 20 μM of SB431542, 0.1 μM LDN193189, 3 μM CHIR-99021, 10 μM AA and 100 nM of Retinoic Acid (RA, Sigma, #R2625- 50MG). At Day 4, medium was changed for N2B27 supplemented with 20 μM of SB431542, 0.1 μM of LDN193189, 10 μM AA, 100 nM of RA and 500 nM of SAG (SIGMA, #566660). At Day 7, cells were cultured in N2B27 medium plus AA (10 μM), RA (100 nM) and SAG (500 nM). At Day 9, 10 μM of DAPT (Tocris, #2634) was added to the day 7 differentiation medium. At Day 11, EBs were dissociated in N2B27 medium supplemented with 10 μM ROCK inhibitor Y-27632, and then seeded on poly-L-ornithin (20 μg/ml, Sigma #P3655)/ Laminin (5 μg/ml, Thermofisher Scientific,#23017-015) or Matrigel (Corning, #354248) coated plates and cultured in N2B27 supplemented with 10 μM AA, 100 nM RA, 500 nM SAG, 10 μM DAPT, BDNF (Peprotech #450-02-10MG) and GDNF (Peprotech, #450-10-10MG), both at 10 ng/ml final concentration. At Day 14, SAG was removed, and the following days until Day 30, the medium (N2B27 supplemented with 10 μM AA, 100 nM RA, 10 μM DAPT, BDNF (10 ng/ml) and GDNF (10 ng/ml)) was changed every other day.

During the differentiation protocol, commitment to mature spinal MN identity was monitored by immunolabeling of markers characteristic of i) spinal MN progenitors (OLIG2), ii) canonical "mature" MN identity (transcription factors ISLET1 and HB9) and iii) more mature cholinergic MNs (CHAT, choline acetyl transferase, the rate-limiting enzyme for acetylcholine) (Davis-Dusenbery et al., 2014) at differentiation day 18 (DIV18) and 30 (DIV30) (Fig. 1A–C). For each experiment, differentiation efficiency was assessed by HB9 and ISLET1 immunostaining as described (Maury et al., 2015). Neurites were labelled using antibody to the neurofilament Medium chain (NF-M), a neuronal cytoskeletal protein.

2.4. Culture of C2C12 myoblasts

C2C12 myoblasts were cultured in Dulbecco's modified Eagle's medium (DMEM) (Thermofisher Scientific, #31966021) supplemented with 10% fetal bovine serum (ThermoFisher Scientific, #10270098) and a mix of antibiotics (penicillin, streptomycin) and antimycotic (Amphotericin B) from ThermoFisher Scientific (antibiotic-antimycotic # 15240062) in a 37 °C incubator stabilized at 5% CO2 until day of co-

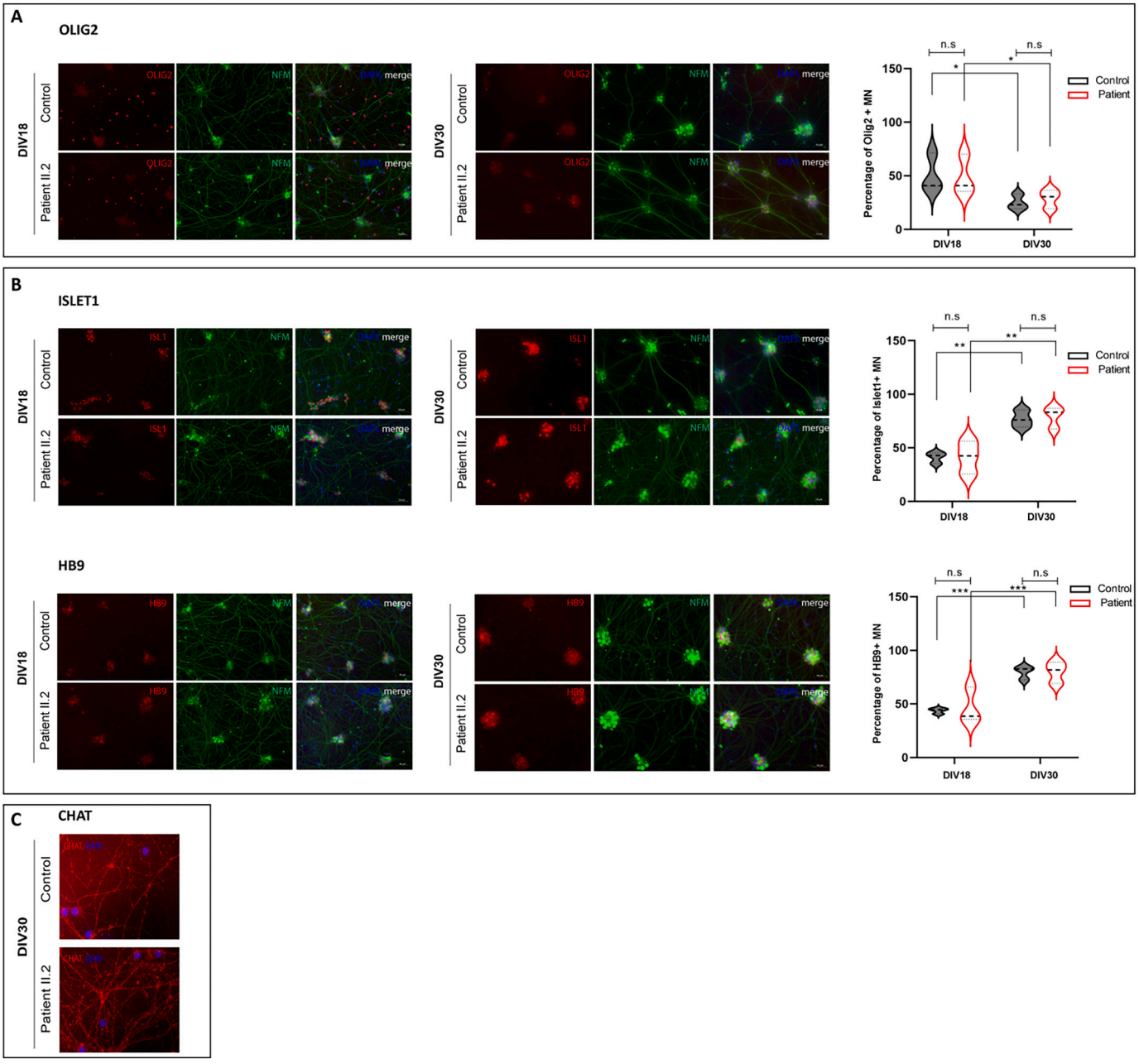

Fig. 1. Monitoring of hiPSC differentiation to spinal Motor Neurons (hiPSC-MNs).
A. *(Left Panel)* Immunolabeling of OLIG2, oligodendrocyte lineage transcription factor 2, a MN progenitor marker, in hiPSC-MNs from patient II.2 and control showing a decrease in OLIG2+ cells at differentiation day 30 (DIV30) as compared to differentiation day 18 (DIV18) in both individuals. NF-M: neurofilament medium chain. *(Right Panel)* Quantification of OLIG2+ neurons (NF-M+) was performed using data from three independent experiments. For each experiment, a mean of 432 and 602 cells at DIV18, and 521 and 584 cells at DIV30, were counted in the control and patient II.2 respectively. The data show a significant decrease of 41% and of 51% of OLIG2+ neurons between DIV18 and DIV30 in patient II.2's and control's hiPSC-MNs respectively. Statistical significance was evaluated by a two-way ANOVA test, $^{*}P < 0.05$, n.s: not significant. Data are represented as violin plots, with median, first and third quartiles **B.** *(Left Panels)* Immunolabeling of transcription factors ISLET1 and HB9 in hiPSC-MNs from patient II.2 and a control showing an increase in HB9 +/ ISLET1 + cells at differentiation day 30 (DIV30) as compared to differentiation day 18 (DIV18) in both individuals. NF-M: Neurofilament medium chain. *(Right Panels)* Quantification of ISLET1+ neurons and HB9+ neurons (NFM+) was performed, using data from three independent experiments. For ISLET1, a mean of 881 and 876 cells at DIV18, and 1342 and 1108 cells at DIV30, were counted in each experiment, in the control and patient II.2 respectively. For HB9, we counted a mean of 745 and 780 cells at DIV18 and 1541 and 1115 cells at DIV30, in each experiment, in control and patient respectively. The data show a significant increase of 48% and of 47% of ISLET1+ neurons and of 42% and of 45% of HB9+ neurons in patient II.2's and control's hiPSC-MNs respectively. Statistical significance was evaluated by two-way ANOVA test, $^{***}P < 0.0005$, n.s: not significant. Data are represented as violin plots, with median, first and third quartiles **C.** Immunolabeling of choline acetyl transferase (CHAT) in hiPSC-MNs from patient II.2 and control at DIV30 suggest that hiPSC-MNs at DIV30 are functional. Quantification of HB9+ (NFM+)/CHAT+ neurons was performed, using data from two independent experiments. A mean of 213 (180 HB9+) and 239 (195 HB9+) cells were counted at DIV30 in the control and patient II.2 respectively.

culture.

2.5. Co-cultures of hiPSC-MNs and C2C12 myoblasts

At 7 days of culture (DIV7), C2C12 myoblasts were detached by trypsinization and 100,000 cells were plated at the top of hiPSC-MNs at day 25 of differentiation (DIV25) cultured on Matrigel-coated 6-well plates or 35 mm dishes, as described in the section "Differentiation of hiPSCs into spinal Motor Neurons". Co-cultured cells were then maintained, during 7 days, in a medium composed of equal volumes of modified C2C12 differentiation medium (DMEM, 2% horse serum (Sigma-Aldrich, #H1270),1% antibiotic-antimycotic (ThermoFisher Scientific, #15240062) and the Motor Neuron differentiation medium used from Day14 to Day30 in the section "*Differentiation of hiPSCs into spinal Motor Neurons (hiPSC-MNs)*". This allowed to reach 14 days of differentiation for the myotubes and 32 days for the hiPSC-MNs.

2.6. In vitro electrophysiological recordings of hiPSC-MNs

Electrophysiological data from patch-clamp recordings in whole-cell configuration were acquired and digitized at 10 kHz in voltage-clamp and current-clamp modes through a Digidata 1440a interface using Clampex 10 software (Molecular Devices). hiPSC-MNs were visualized with infrared differential interference contrast microscopy using a Nikon Eclipse E600FN upright microscope coupled with a water-immersion objective (Nikon Fluor 40×/0.8 W). Whole-cell patch-clamp recordings were made from hiPSC-MNs without co-cultured myoblasts (DIV18-DIV39) or hiPSC-MNs cocultured with myoblasts (DIV18-DIV32) selected on the basis of their large cell bodies (>20 μm), their distinct processes and their hyperpolarized resting membrane potential (<-65 mV). The image was enhanced with a Hitachi KP-200/201 infrared-sensitive CCD camera and displayed on a video monitor. Whole-cell patch-clamp recordings in current-clamp mode were performed with a Multiclamp 700B amplifier (Molecular Devices). Patch electrodes (2–5 MΩ) were pulled from borosilicate glass capillaries (1.5 mm OD, 1.12 mm ID; World Precision Instruments) on a Sutter P-97 puller (Sutter Instruments) and filled with intracellular solution containing the following (in mM): 140 K^+-gluconate, 5 NaCl, 2 MgCl2, 10 HEPES, 0.5 EGTA, 2 ATP, 0.4 GTP, pH 7.3. In the recording chamber, hiPSC-MNs were continuously bubbled with 95% O_2 / 5% CO_2, heated (32–34 °C) and perfused with ACSF containing the following (in mM): 120 NaCl, 3 KCl, 1.25 NaH_2PO_4, 1.3 $MgSO_4$, 1.2 $CaCl_2$, 25 $NaHCO_3$, 20 D-glucose, pH 7.3–7.4.

2.7. Measurement of electrophysiological properties

Electrophysiological data were analyzed with Clampfit 11 software (Molecular Devices). Passive membranes properties of cells were measured by determining from the holding potential the largest voltage deflections induced by small currents pulses to avoid the activation of voltage-sensitive currents. The input resistance was measured by the slope of the linear portion of the I/V relationship. The rheobase was defined as the minimum current intensity necessary to induce action potential during a 1-s pulse. We measured the AP waveform properties of the first AP from a train of spikes in response to a long-duration (7.5 s) depolarizing current pulse at 1.7× rheobase by using the Event Detection/Threshold Search module of Clampfit 11.0.3. Peak spike amplitude was measured from the threshold potential, and spike duration was defined as the time to fall to half-maximum peak. The peak amplitude of the afterhyperpolarizations (AHPs) following the first spike was also measured. Firing patterns in response to a long-duration (7.5 s) depolarizing current pulse (1.7× rheobase) were assigned to four categories (stable, increasing, decreasing, bursting) based on (1) the analysis of the mean firing frequency overtime and (2) the quantification of the squared coefficient of variation of the interspike interval (CV2). We also determined whether the cells displayed a delay to first spike or if they were instantaneously firing in response to a long-duration (7.5 s) depolarizing current pulse at rheobase.

2.8. Measurement of the fast, inactivating Na+ currents

We measured the peak Na+ currents of hiPSCs-MNs in presence of the broad-spectrum voltage-gated K^+ channels blocker (tetraethylammonium chloride, TEA, 10 mM) and the broad-spectrum voltage-gated Ca^{2+} channels blocker (Cadmium, Cd^{2+}, 30-50 μM) in response to a series of voltage steps (−70 to 5 mV, 2.5 mV increments, 600 ms duration) from a holding potential of −60 mV. In some experiments, we added the voltage-gated Na + channels blocker (tetrodotoxin, TTX, 0.5 μM) to block the fast inactivating Na+ currents.

2.9. Immunostaining and microsocopy

At Day30 of differentiation (DIV30), hiPSC-MNs, grown on coverslips in four or six well matrigel coated plates were washed with Dulbecco's Phosphate Buffer Saline buffer (PBS) and fixed in 4% paraformaldehyde in PBS for 15 min. Cells were then washed for 10 min in PBS and were permeabilized using 0.1% Triton X-100 in PBS for 10 min at room temperature. After blocking for 30 min at room temperature in PBS containing 0.1%Triton X-100 and 1% Bovine Serum Albumin (BSA), hiPSC-MNs were incubated overnight at 4 °c with the primary antibodies diluted in the blocking solution. Primary antibodies used were: rabbit polyclonal to Olig-2 (Merck Millipore, #AB9610) (dilution 1:500), Mouse monoclonal to Islet-1 (Biorbyt, #Orb95122) (1:200), mouse monoclonal to HB9 (DSHB, #81.5C10) (1:40), goat polyclonal to CHAT (Merck Millipore, #AB144p) (1:200), Chicken polyclonal to NF-M (Biolegend, #PCK-593P) (1:1000), rabbit polyclonal to Dysferlin (abcam, #ab124684) (1:200), and mouse monoclonal to Ankyrin-G (NeuroMab, clone N106/36) (1:500).

After 3 washes in PBS, cells were incubated for 2 h with the appropriate secondary antibody, in the blocking solution at room temperature, in the dark. The following secondary antibodies were used at 1:1000 dilution: donkey Anti-Goat IgG H&L (DyLight® 594) (abcam, #ab96933), donkey Anti-Mouse IgG (DyLight® 550) (abcam, #ab96876), donkey Anti-Rabbit IgG (DyLight® 550) (abcam, #ab96892), goat anti-Chicken IgY H&L (Alexa Fluor® 488) (abcam, #ab150169).

The samples were then mounted in Vectashield mounting medium (Vector Laboratories, #H-2000) with 100 ng/ml DAPI (4,6-diamidino-2-phenylindole), coverslipped, and sealed. Digitized microphotographs were recorded using an ApoTome fluorescent microscope (ZEISS, Germany), equipped with an AxioCam MRm camera. These images were merged with the ZEN software, and were treated using ImageJ software (National Institutes of Health, MD, USA).

2.10. Measurement of AIS length and intensity

AIS length and intensity were measured on hiPSC-MNs after AnkyrinG immunolabeling, as described in the previous paragraph. AIS length and intensity were measured using ImageJ software. AIS length was defined by the length of the AnkyrinG+ segment and AIS intensity was calculated by measuring the relative intensity of the specified AnkyrinG+ area. Data for both length and intensity were recorded from three independent experiments.

3. Results

3.1. Differentiation of hiPSCs into spinal Motor Neurons (hiPSC-MNs)

We observed no differences in the expression of OLIG2, HB9 and ISLET1 between patient and control hiPSC-MNs, either at DIV18 or DIV30 (Fig. 1A–C). At DIV18 half of NF-M positive cells (NF-M+) expressed OLIG2 (50.7% for control and 48.8% for patient II.2)

(Fig. 1A), while only 41 to 46% of NF-M + cells were positive for HB9 and ISLET1, the generic markers of spinal MNs (Fig. 1A–C). At DIV30, the majority (up to 80%) of neurons (NF-M + cells) were already expressing HB9 and ISLET 1, whereas OLIG2 has decreased by half, confirming the ventral spinal cord identity and the acquisition of a "mature" MN phenotype at DIV30. Furthermore, both in control and patient, at DIV30, all "mature" (HB9+/ISLET1+) cells expressed Choline Acetyltransferase (CHAT), the rate-limiting enzyme for acetylcholine, suggesting that they are likely to be functional (Fig. 1D).

3.2. Electrophysiological properties of hiPSC-MNs with or without co-culture with myoblasts

Motoneurons are distinguished from interneurons by their larger size and a more hyperpolarized resting membrane potential (Tazerart et al., 2007). Whole-cell recordings on putative hiPSC-MNs were thus performed on the largest neurons displaying both a body cell above 20 μm and a resting membrane potential below -65 mV (Fig. 2, Table 1). Before DIV30, neurons did not fire repetitively. These immature cells displayed either one single AP (DIV18) or a transient firing with few APs (DIV29) in response to pulse or sinusoidal depolarizing currents lasting several seconds (Fig. 2A and B).

In order to obtain further maturation of hiPSC-MNs *in vitro,* we maintained cultures for at least 2 additional days. Interestingly, we noticed that, unlike before DIV30, the vast majority (~82%) of hiPSC-MNs above DIV30 were able to generate a robust repetitive spiking during the whole duration of the current pulse (Fig. 2C–E). However, maintaining hiPSC-MNs in culture for more than 30 days is very challenging, because of cells detaching from their support. On the other hand, it is well known that MNs and muscle cells have mutual stabilizing and supportive influence to each other (Maffioletti et al., 2018; Mazaleyrat et al., 2020; Yoshida et al., 2015), and therefore, we sought to increase the viability and functionality of our hiPSC-MNs by coculturing them with mouse myoblasts (C2C12) for 7–9 days. This allowed obtaining large multinucleated myoblasts, and hiPSC-MNs extending long neurites alongside the myoblasts (Supplementary Fig. 1). Similarly to what was observed in DIV36 hiPSC-MNs without coculture (Fig. 2C–D, left), and unlike hiPSC-MNs without co-culture before DIV30 (Fig. 2A–B, right), the vast majority (~89%) of DIV32 hiPSC-MNs cocultured with myoblasts (Fig. 2C–D and F, right) show a mature electrophysiological phenotype and were able to sustain their firing rate without spiking inactivation in response to a prolonged depolarizing current (Fig. 2D, top right) or in response to sinusoidal current pulses of same amplitudes (1 Hz, 80pA) (Fig. 2D, bottom right). The functional maturation of sustained firing hiPSC-MNs after DIV30 was mainly characterized by two criteria: (1) the hyperpolarization of the resting membrane potential and (2) the increase of the AP amplitude compared to immature cells (Fig. 2G–H). Note that before DIV30, none of the hiPSC-MNs were able to generate sustained spiking activity: 75% of them display an immature AP (peak amplitude <40 mV), 15% a single AP (peak amplitude >40 mV) and 10% a short train of spikes (Supplementary Fig. 2A). After DIV30, only 15% of the hiPSC-MNs displayed an immature firing pattern mainly characterized a transient spiking activity (Supplementary Fig. 2B).

3.3. Functional subtypes diversity of hiPSC-MNs

We next tested the functional properties of mature hiPSC-MNs, either without coculture at DIV36, or at DIV32 when co-cultured for 7 days with C2C12 primary mouse myoblasts. In the latter, we specifically observed regular high-frequency contractions of myoblasts (Movie S1). Both co-cultured and not co-cultured hiPSC-MNs display four distinct electrophysiological signatures (Fig. 3A–D): one with a voltage-dependent oscillatory firing characterized by an increase of the oscillations frequency (gray traces) as a function of the current pulse intensity (Fig. 3A–B) and three others displaying repetitive spiking which were distinguished by a stable (Fig. 3C–D, left), increased (Fig. 3C–D, middle) or decreased (Fig. 3C–D, right) firing frequency at 1.7× the rheobase. This subtypes classification was based on the analysis of the mean firing frequency over time (Fig. 3D) and the quantification of the squared coefficient of variation (CV2) of the interspike interval (Fig. 3E). Contrary to stable firing cells which displayed a constant firing over time (Fig. 3D, left) with a CV2 of inter-spike interval close to zero (Fig. 3E), all other subtypes exhibited variation of their firing rate over time (Fig. 3D) and significant higher CV2 values (Fig. 3E). Thus, we were able to distinguish 15%, 17%, 45% and 23% of hiPSC-MNs with stable, increased, decreased and bursting firing, respectively (Fig. 3F). When recorded at rheobase, almost all cells (~96%) from the 4 distinct subtypes displayed a delay (813 ± 180.4 ms) to first spike (Fig. 3G). Taken together, these data indicate that the diversity of the hiPSC-MNs subtypes is a hallmark of functional maturity.

3.4. Electrophysiological properties of hiPSC-MNs from patients with VRK1 mutations

To determine if mutations in *VRK1* described previously by us in two patients affected with autosomal recessive distal Hereditary Motor Neuropathy (dHMN) (El-Bazzal et al., 2019), affect the electrical properties of the spinal motor neurons, we recorded, in whole-cell configuration, the firing pattern of hiPSC-MNs from one patient (patient II.2, see (El-Bazzal et al., 2019) from DIV30 to DIV39, with or without co-culture with myoblasts. We first observed that the patient's hiPSC-MNs display the four firing patterns similar to those described in control (Fig. 4A–D). We also showed that the proportion (~74%) of mature hiPSC-MNs with a sustained firing from patient II.2 (Fig. 4E) was similar to controls (Fig. 2E–F). The four distinct firing patterns were also present in approximatively the same proportion (Fig. 4F) than controls (Fig. 3F). In addition, we observed that the patient's hiPSC-MNs displayed a delay (1102 ± 233.9 ms) to first spike at the rheobase (Fig. 4G) in the exact same proportion (~96%) than controls (Fig. 3G). Also, neither the firing gain nor the maximum instantaneous firing frequency were significantly affected in each subtype of the patient's hiPSC-MNs (Fig. 4H–I).

3.5. AP waveform of hiPSC-MNs from patients with VRK1 mutations

In the patient's hiPSC-MNs, when pooling all the subtypes, we quantified a significant decrease of AP amplitude, rise slope and decay slope, in all distinct subtypes, accompanied by an increase of AP duration and a decrease of the AHP amplitude (Fig. 5A–B and Table 1). To investigate the mechanisms underlying this significant decrease in AP amplitude, we next performed voltage-clamp recordings of the voltage-activated Na^+ currents for each subtype. We investigated the fast, inactivating Na^+ currents which were TTX-sensitive (Supplementary Fig. 3). We observed a strong decrease in the peak Na^+ currents for each subtype (Fig. 5C–D, Table 1) which becomes significant when we pool all subtypes. We also noticed a strong difference in the current-voltage (I-V) relationships between MNs derived from patients and control hiPSCs for each subtype (Fig. 5E). In sum, although the firing pattern of the patient's hiPSC-MNs was similar to control, there is a significant change in the shape of the Action Potential (AP) observed in all distinct subtypes, which appears to be related to a decrease of the voltage-activated Na^+ currents (Fig. 5A–B and Table 1).

3.6. Reduced Axonal Initial (AIS) length in hiPSC-MNs from a patient with VRK1 mutations

Previous studies performed in patient II.2's hiPSC-MNs have shown impaired neurite length and branching in patient's hiPSC-MNs as compared to a control (El-Bazzal et al., 2019). Knowing that the AP waveform is closely linked to the Axonal Initial Segment (AIS) length (Kaphzan et al., 2011; Kuba, 2012), we sought to investigate if the modified AP amplitude observed in patient's MNs is linked to a

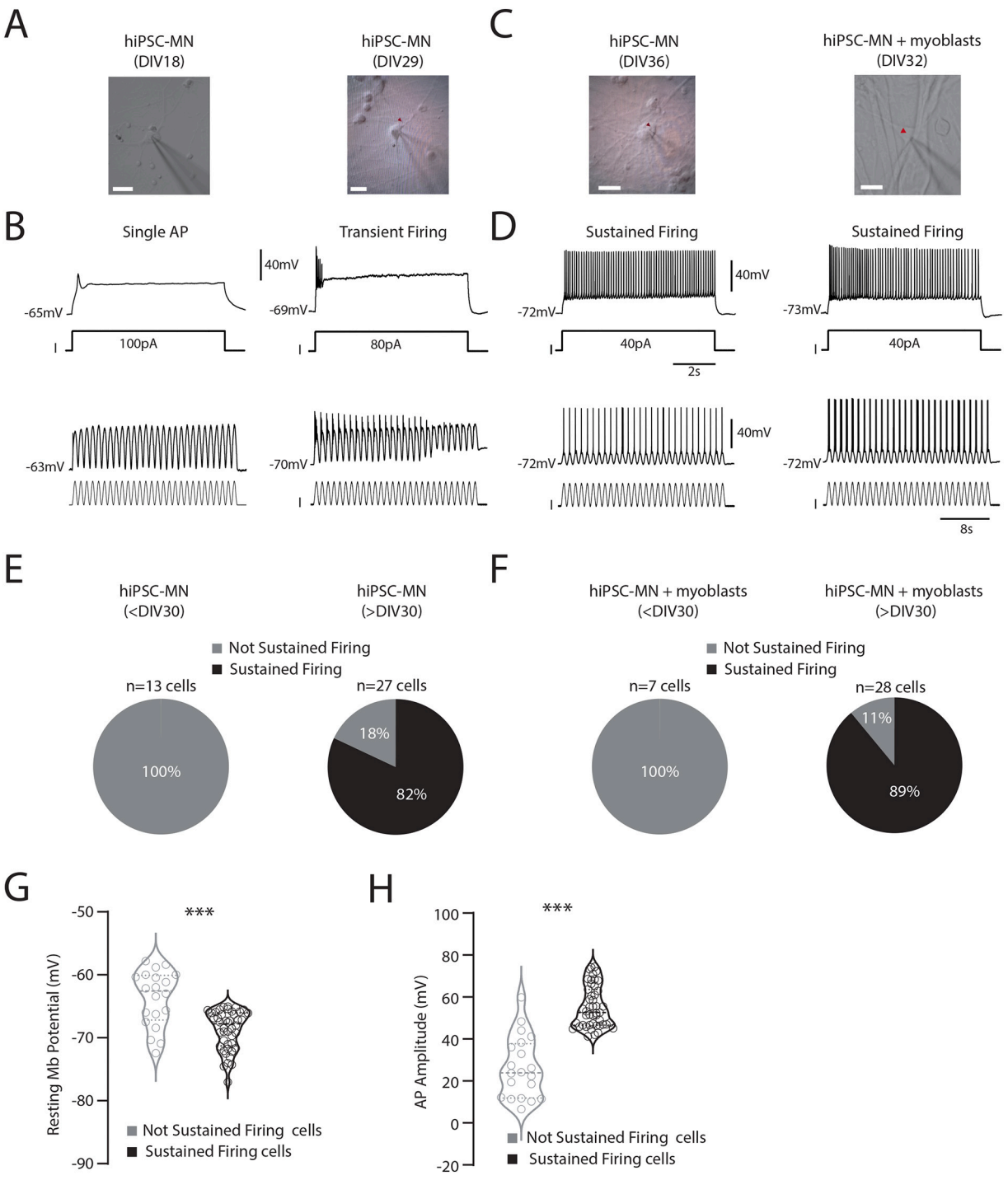

Fig. 2. Co-culturing human hiPSC-MNs with myoblasts accelerates their functional maturation.
A. Bright field images of hiPSC-MNs at DIV18 (left) or DIV29 (right) in presence of the intracellular pipette for Patch-Clamp recordings. **B**. Representative voltage traces of two hiPS-MNs illustrated above in response to long-lasting (7.5 s) depolarizing current pulses (top) or sinusoidal current pulses (1 Hz,30s) (bottom). **C.** Bright field images of hiPSC-MNs at DIV36 (left) or DIV32(right) without (left) or with (right) co-culture with mouse myoblasts (C2C12), respectively. The red mark indicates the recorded MN in whole-cell configuration. **D**. Representative voltage traces of two mature hiPS-MNs without (left) or with (right) co-culture with mouse myoblasts (C2C12), illustrated above, in response to long-lasting (7.5 s) depolarizing current pulses (top) or sinusoidal current pulses (1 Hz,30s) (bottom). **E–F**. Proportion of hiPS-MNs without (**E**) or with (**F**) co-culture with mouse myoblasts (C2C12), before (left) or after (right) DIV30, displaying a sustained/bursting firing (black) or not firing (gray) in response to a long-lasting (7.5 s) depolarizing current pulse. **G–H**. Violin plots of resting membrane potential (**G**) and AP amplitude (**H**) of hiPSC-MNs co-cultured, or not, with mouse myoblasts before (left) or after (right) DIV30 (***, $p < 0.001$, Mann–Whitney test). (For interpretation of the references to color in this figure legend, the reader is referred to the web version of this article.)

Table 1
Action potential and firing parameters from hiPSC-MNs.

	Stable		Increased		Decreased		Bursting		All cells	
	Control	Patient II.2	Control	Patient II.2	Control	Patient II.2	Control	Patient II.2	Control	Patient II.2
N	7	4	8	5	21	12	11	7	47	28
Vrest (mV)	−68.6 ± 2.8	−65 ± 3.3	−68.6 ± 2.8	−64.5 ± 3.3	−68.8 ± 2.2	−71.6 ± 1.1	−69.8 ± 4.2	−70.2 ± 1.9	−68.5 ± 1.2	−69.7 ± 1.2
Rin (MΩ)	426.4 ± 115.2	508.1 ± 131.4	417.3 ± 143.7	593.8 ± 144.9	490.8 ± 66.6	462.2 ± 91.1	550.9 ± 107.4	822.3 ± 79.1	482 ± 47.7	586.4 ± 58.4
AP amplitude (mV)	55.9 ± 3.4	39.3 ± 2.8 *	61.7 ± 3.1	40.6 ± 2.4 **	55.5 ± 2.2	43.1 ± 0.9 ***	46.1 ± 1.7	36.6 ± 2.2 *	54.8 ± 1.5	40.5 ± 0.9 ***
Peak Na + current ampl. (pA)	−2162 ± 786.9 (n = 3)	−1355 ± 339.7 (n = 5)	−3579 ± 1037 (n = 3)	−1120 ± 310.9 (n = 6) *	−3147 ± 1214 (n = 5)	−1031 ± 185.4 (n = 5)	−2924 ± 735.1 (n = 3)	−1317 ± 512.1 (n = 6)	−2981 ± 503.4 (n = 14)	−1248 ± 178 (n = 22) ***
AP half width (ms)	1.3 ± 0.1	1.5 ± 0.2	1.5 ± 0.1	1.7 ± 0.2	1.3 ± 0.1	1.6 ± 0.1	1.4 ± 0.1	1.7 ± 0.2	1.3 ± 0.05	1.6 ± 0.09 *
AP rise slope (mV/ms)	46.3 ± 7.9	24.5 ± 5.1	37.4 ± 7.9	22.1 ± 7.3	57.3 ± 5.4	26.9 ± 4.4 ***	33.6 ± 7.1	28.3 ± 5.6	47.3 ± 3.6	26.0 ± 2.7 ***
AP decay slope (mV/ms)	−14.0 ± 2.5	−7.5 ± 1.8 *	−9.7 ± 1.5	−7.2 ± 1.6	−13.3 ± 1.4	−9.3 ± 1.5	−6.3 ± 1.0	−5.1 ± 0.6	−11.4 ± 0.9	−7.6 ± 0.8 **
AP threshold (mV)	−50.2 ± 2.7	−38.2 ± 3.1 *	−51.7 ± 2.9	−47.8 ± 1.7	−48.3 ± 1.6	−47.3 ± 0.9	−48.6 ± 1.3	−46.3 ± 1.4	−49.2 ± 0.9	−45.8 ± 0.9 *
Rheobase (pA)	30.7 ± 9.6	22.5 ± 10.9	25 ± 4.3	14.8 ± 3.3	24.7 ± 3.6	30.1 ± 6.1	17.8 ± 4.4	5.6 ± 1.0	24.0 ± 2.5	20.1 ± 3.5
AHP amplitude (mV)	−11.1 ± 1.9	−8.9 ± 1.3	−9.8 ± 1.6	−9.3 ± 1.4	−9.6 ± 0.7	−6.2 ± 0.8 **	−6.7 ± 0.6	−4.3 ± 0.8 *	−9.2 ± 0.6	−6.7 ± 0.6 *
Gain (Hz/pA)	0.26 ± 0.07	0.26 ± 0.12	0.32 ± 0.14	0.21 ± 0.06	0.29 ± 0.04	0.37 ± 0.09	0.54 ± 0.12	0.72 ± 0.17	0.35 ± 0.04	0.43 ± 0.07
Max Firing rate (Hz)	23.0 ± 3.6	25.9 ± 6.1	12.3 ± 2.4	14.8 ± 4.1	28.6 ± 2.9	31.0 ± 3.5	28.7 ± 3.1	28.0 ± 5.4	25.2 ± 1.8	26.9 ± 2.5

Data are mean ± sem. *p < 0.05; **p < 0.01, ***p < 0.001 Mann-Whitney test.
Vrest: resting membrane potential; AP: action potential; AHP: afterhyperpolarization, Rin: input resistance; ISI: inter-spike interval.

modification in the AIS of those MNs. To do so, we have performed immunolabeling of AnkyrinG, a scaffold protein, known as the master organizer of the AIS, in patient's and control's hiPSC-MNs (Fig. 6A). While we showed no differences in the intensity of the AIS (Fig. 6C), we observed a significant decrease in AIS length (~40%) in the patient's MNs as compared to the control (Fig. 6B).

4. Discussion

In this study, we show that MNs derived from human iPSCs obtained from healthy individuals or patients harbouring *VRK1* mutations develop similar electrophysiological firing subtypes. However, patient's hiPSC-MNs display APs of shorter amplitude and larger duration. This modification is likely to result from a decrease in the peak Na+ currents accompanied by a decrease in the AIS length. These data from human MNs indicate that mutations in *VRK1* contribute to the alteration of the action potential waveform that may ultimately lead to the upper and motor neuron disease affecting these patients.

We recently described new mutations in *VRK1*, the vaccinia-related kinase 1 gene, in patients affected with a distal form of Charcot-Marie-Tooth disease (dHMN, for distal Hereditary Motor Neuropathy) associated with upper motor neuron signs (El-Bazzal et al., 2019). Mutations in the *VRK1* gene are responsible for a wide spectrum of autosomal recessive neurological diseases, ranging from Hereditary Sensory-Motor Neuropathy (Charcot-Marie-Tooth disease) (Gonzaga-Jauregui et al., 2013) to juvenile ALS (Nguyen et al., 2015). All these diseases have in common the involvement of lower MNs. *VRK1* encodes the Vaccinia Related kinase 1, a 396 amino acid (aa), ubiquitously expressed, serine/threonine kinase, playing a crucial role in regulating cell cycle (Valbuena et al., 2008, 2011). VRK1 is mainly a nuclear protein, although the presence of a small fraction in the cytoplasm and membrane compartments has been described (Nichols and Traktman, 2004; Valbuena et al., 2007). Several substrates are known, to date, for VRK1 (El-Bazzal et al., 2019), including VRK1 (Lopez-Borges and Lazo, 2000), and coilin, the main component of Cajal Bodies (CBs) (Sanz-Garcia et al., 2011).

Although it is now evident that the motor tract is mainly affected in patients with mutations in *VRK1*, little is known whether mutations in this gene directly alter the functional properties of MNs. We previously demonstrated, in human patient's iPS-derived MNs (hiPSC-MNs), that mutations in *VRK1* cause a drop in VRK1 levels leading to Cajal Bodies (CBs) disassembly and to defects in neurite outgrowth and branching (El-Bazzal et al., 2019). We assumed that these changes were likely to drive a modification in cell excitability (Gulledge and Bravo, 2016). Therefore, here, we tried to answer the question whether these structural changes affect the firing pattern of hiPSC-MNs, by performing electrophysiological measurements in hiPSC-MNs from patients with mutations in VRK1. First, we confirmed that the differentiation protocol used to obtain spinal MNs from hiPSCs (Maury et al., 2015) induces functional MNs, by testing the capacity of control hiPSC-MNs to spike in response to the injection of a current depolarizing step or repetitive oscillations. Our hiPSC-MNs showed mature phenotypes characterized by sustained firing pattern, typical of spinal motoneurons (Bos et al., 2018; Durand et al., 2015; Gao and Ziskind-Conhaim, 1998; Smith and Brownstone, 2020; Vinay et al., 2000). In addition to sustained firing patterns, mature hiPSC-MNs displayed hyperpolarized resting membrane potentials accompanied with an increase in AP amplitude compared to immature cells. This functional maturation occurs ~4–5 weeks post-plating, as it has been previously shown in cultured human iPSC-derived MNs (Liu et al., 2015; Maury et al., 2015; Saporta et al., 2015), confirming the functionality of the recorded hiPSC-MNs.

We also demonstrated that hiPSC-MNs co-cultured with mouse myoblasts enhance their functional maturation by displaying sustained firing ~ one week earlier than MNs cultures alone. This result suggests the presence of bidirectional interactions with muscle cells (Sances et al., 2016; Bucchia et al., 2018) confirmed by the presence of muscle contractions likely occurring when hiPSC-MNs were firing, although we cannot totally exclude simple spontaneous contraction. Because spinal motor neurons display distinct sustained firing pattern (Durand et al., 2015; Hadzipasic et al., 2014; Manuel and Zytnicki, 2019), we tested whether hiPSCs-MNs also display this heterogeneity of activity pattern. Thus, we were able to clearly demonstrate the presence of distinct subtypes in sustained firing hiPSC-MNs co-cultured with muscle cells suggesting that our recorded hiPSC-MNs are fully mature. This cue of functional maturity was crucial to obtain in order to compare hiPSC-MNs from healthy individuals with those from patients harbouring VRK1 mutations.

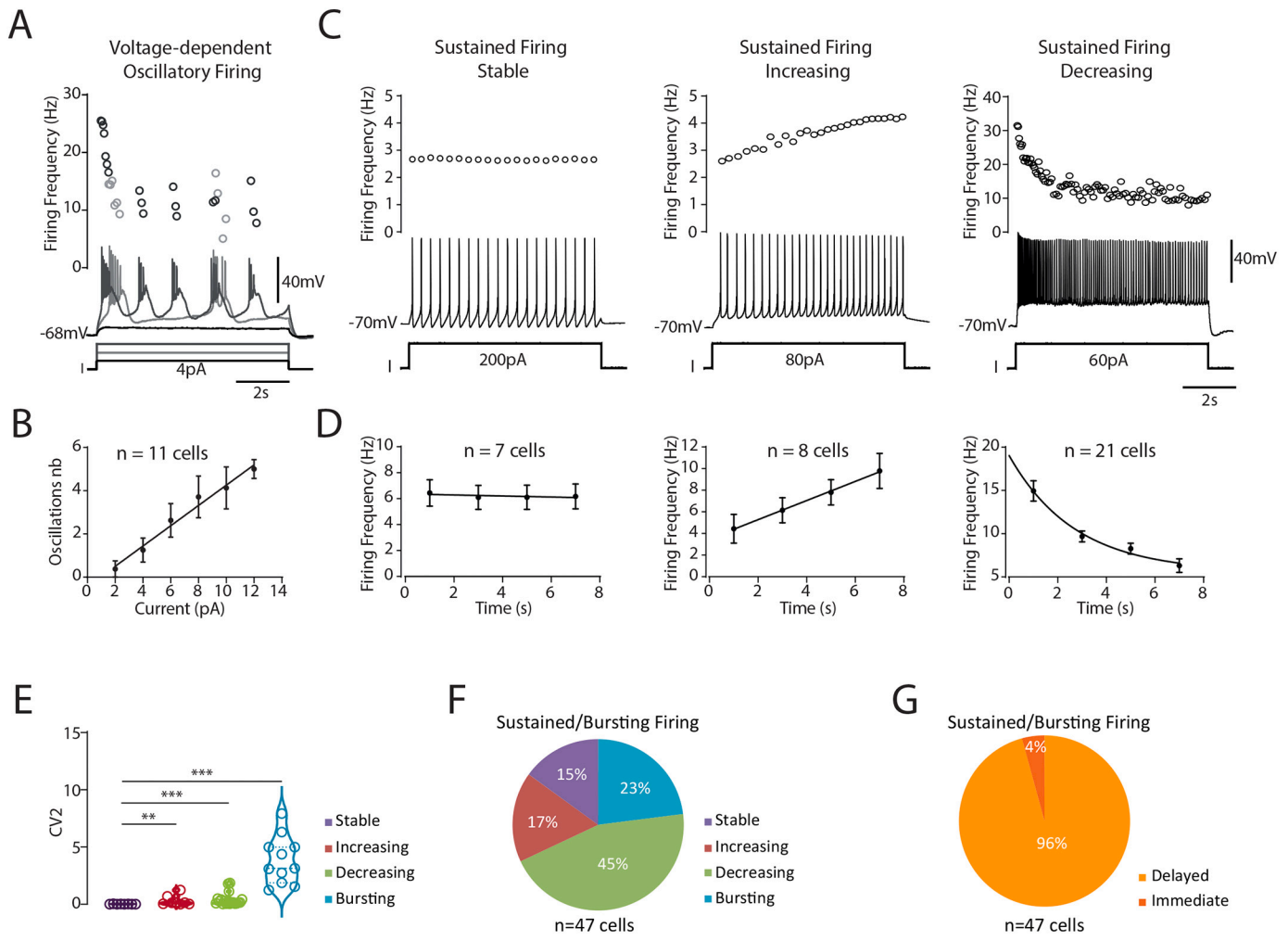

Fig. 3. Mature hiPSC-MNs display four distinct electrophysiological signatures.
A–B. Representative voltage trace (**A**) of one hiPS-MN co-cultured with myoblasts displaying voltage-dependent oscillations (bursting) in response to a long-lasting depolarizing current pulse. (**B**) The frequency of the oscillation numbers increases as a function of the current amplitude. **C–D.** Representative voltage traces (**C**) of three hiPSC-MNs co-cultured with myoblasts displaying sustained spiking in response to long-lasting depolarizing current pulses. They are distinguished in three subtypes as a function of their mean firing frequency overtime (**D**): stable (left, DIV 32), increasing (middle, DIV 32) or decreasing (right, DIV 32). Note the same electrophysiological patterns were recorded in hiPSC-MNs without myoblasts co-culture. **E.** Violin plots of the squared coefficient of variation of the inter-spike interval from each hiPSC-MN subtypes after DIV30. Stable, increasing, decreasing and bursting firing cells are represented in purple, red, green and blue respectively (**, $p < 0.01$, ***, $p < 0.001$, Mann–Whitney test). **F.** Proportion of hiPSC-MNs after DIV30 displaying stable (purple), increasing (red), decreasing (green) and bursting (cyan) firing in response to a long-lasting (7.5 s) depolarizing current pulse. **G.** Proportion of sustained or bursting firing subtypes from control hiPSC-MNs after DIV30 displaying a delay to first spike in response to a long-lasting depolarizing current pulse at rheobase. (For interpretation of the references to color in this figure legend, the reader is referred to the web version of this article.)

Surprisingly, although our patients' hiPSC-MNs show structural changes, such as shorter neurite length and altered branching (El-Bazzal et al., 2019), we did not observe any differences in the firing patterns of hiPSC-MNs from patients harbouring VRK1 mutations compared to healthy individuals.

We, however, demonstrated significant alterations of the shape of individual action potentials, in patients, distinguished by a smaller amplitude and a larger duration. These results are in line with other studies reporting significant changes in the electrophysiological properties of hiPSC-MNs from patients affected with other diseases affecting axons of lower motor neurons (Charcot-Marie-Tooth, CMT2E and CMT2A) (Saporta et al., 2015), lower motor neurons (Spinal Muscular Atrophy) (Liu et al., 2015) or upper and lower motor neurons (Amyotrophic Lateral Sclerosis due to SOD1 or C9ORF72 or TARDBP 2) (Devlin et al., 2015; Wainger et al., 2014).

Indeed, in those studies, all recorded hiPSC-MNs are transiently or chronically hyperexcitable, with hyperpolarized thresholds and larger AP amplitude, reflecting changes in sodium, calcium or potassium channel dynamics. In our case, hiPSC-MNs from patients displayed a depolarized AP threshold and smaller AP amplitude reflecting hypoexcitable state instead of hyperexcitability, although we did not observe any significant modification of firing gain or rheobase. Note that hypoexcitability has recently been proposed to reflect MN firing defects in mouse models of ALS (Filipchuk et al., 2021; Martinez-Silva et al., 2018), in accordance with results obtained in hiPSC-MNs of ALS patients with *C9ORF72* triplet expansions (Sareen et al., 2013). Together with our results, this underlines the need to further explore the mechanistic links between hyperexcitability and hypoexcitability.

The smaller and broader AP recorded in patients with VRK1 mutations is associated with a decrease of the peak Na + currents accompanied by a decrease in the length of the ankyrinG (AnkG)-positive Axonal Initial Segment (AIS). Interestingly, it has been shown that mutant mice lacking AnkG in cerebellar cells develop motor troubles and deficits in initiating AP (Zhou et al., 1998), likely due to decrease of voltage-

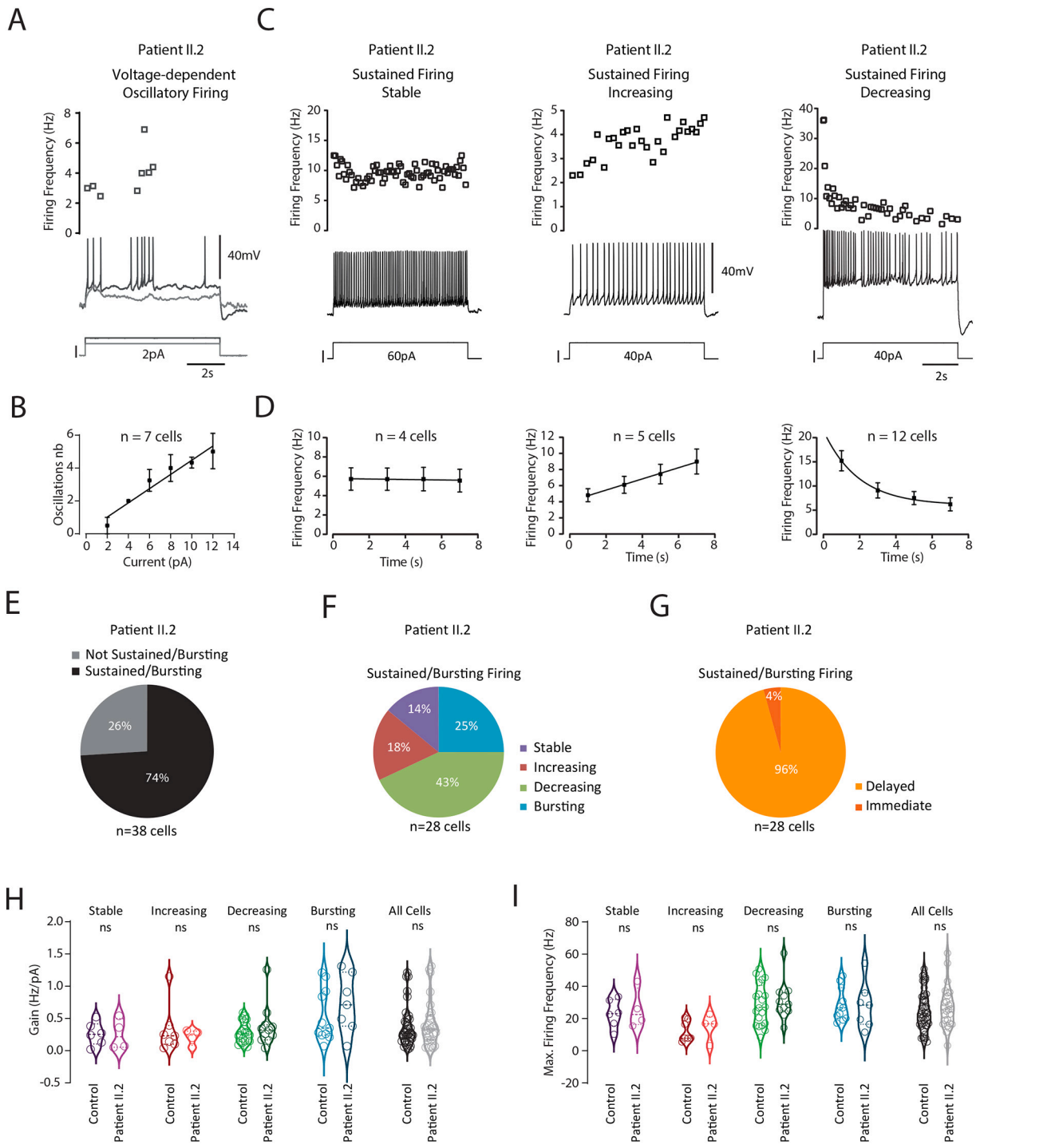

Fig. 4. hiPSC-MNs from patient II.2 display similar electrophysiological firing patterns than controls.
A–B. Representative voltage traces (**A**) of hiPS-MNs (DIV32, cocultured with C2C12 myoblasts) from patient II.2 displaying the voltage-dependent oscillatory firing subtype in response to a long-lasting depolarizing current pulse. The oscillations number as a function of the injected current is represented in (**B**). **C–D.** Representative voltage traces (**C**) of three hiPSC-MNs from patient II.2 displaying sustained stable (left), increased (middle) or decreased (right) firing in response to long-lasting depolarizing current pulses comparable to controls at DIV32 cocultured with C2C12 myoblasts. The mean firing frequency overtime for each subtype is represented in (**D**). **E.** Proportion of hiPS-MNs from patient II.2 after DIV30 displaying a sustained or bursting firing (black) or not (gray) in response to a long-lasting (7.5 s) depolarizing current pulse. **F.** Proportion of distinct firing pattern subtypes from patient II.2 hiPSC-MNs after DIV30 in response to a long-lasting depolarizing current pulse. **G.** Proportion of sustained or bursting firing subtypes from patient II.2 hiPSC-MNs after DIV30 displaying a delay to first spike in response to a long-lasting depolarizing current pulse at rheobase. Fisher test was used to compare the proportions of hIPSC-MNs subtypes between control and patient II.2. **H–I.** Violin plots of the firing gain (**H**) or the maximum instantaneous firing rate (**I**) of each firing subtype from control (left) and patient II.2 (right) mature hiPSC-MNs. (ns, Mann-Whitney test).

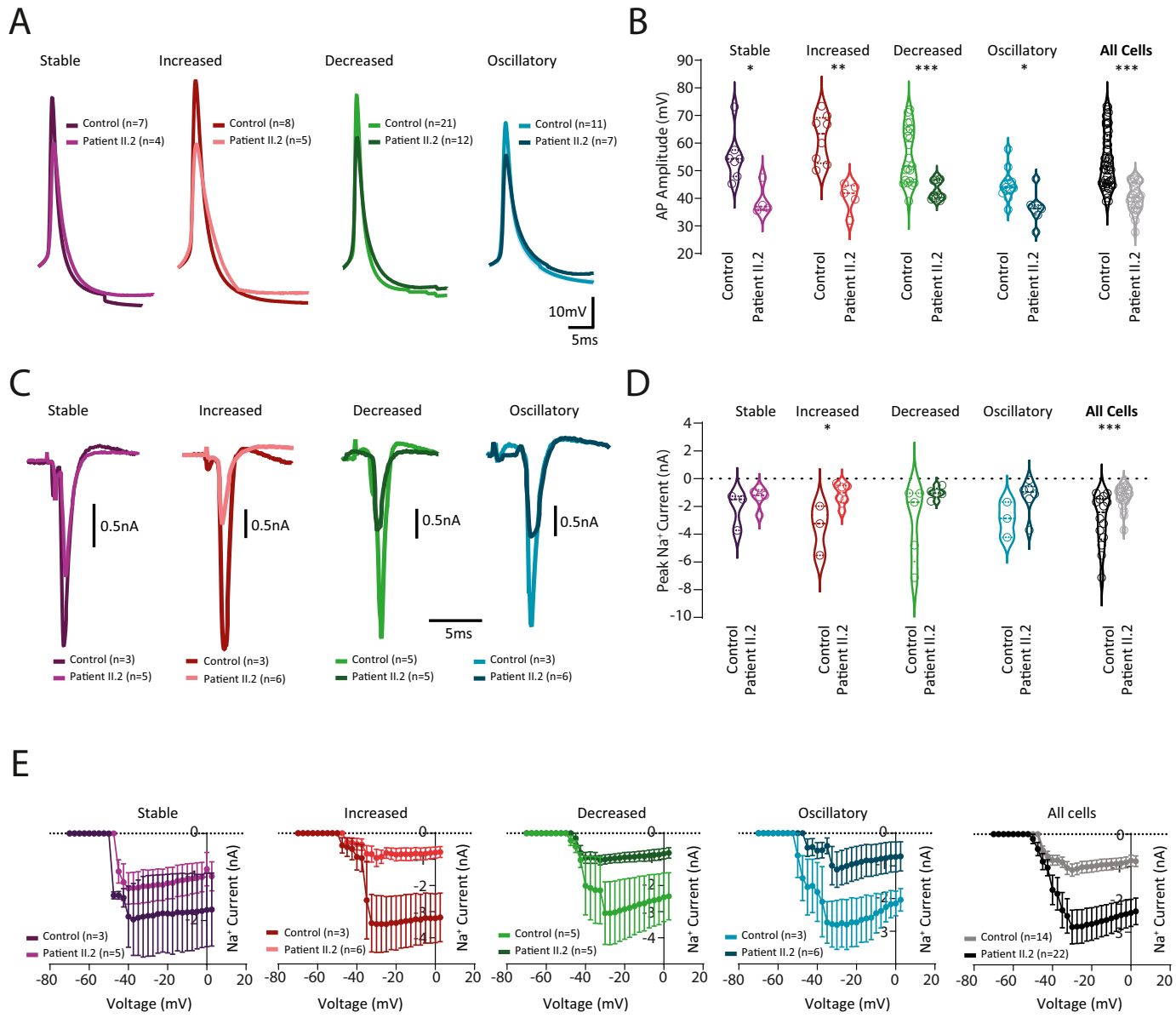

Fig. 5. hiPSC-MNs from patient II.2 display smaller AP accompanied with a decrease or peak Na + currents.
A. Superimposed average traces of the first AP recorded in current-clamp mode from control versus patient II.2 mature hiPSC-MNs subtypes. Color codes are mentioned in the upper right part of the average traces. **B.** Violin plots of the AP amplitude from each subtype of control (left) versus patient II.2 (right) mature hiPSC-MNs. (*, $p < 0.05$; **, $p < 0.01$; ***, $p < 0.001$ Mann-Whitney test). **C.** Superimposed average traces of the peak Na^+ currents recorded in voltage-clamp mode from control versus patient II.2 mature hiPSC-MNs subtypes. Color codes are mentioned in the bottom part of the average traces. **D.** Violin plots of the peak Na^+ currents from each subtype of control (left) versus patient II.2 (right) mature hiPSC-MNs (*, $p < 0.05$ Mann-Whitney test). **E.** Representation of the current-voltage (I-V) relationships between each mature hiPSC-MNs subtype derived from control versus patient II.2.

dependent Na^+ channels (Jenkins and Bennett, 2001). Knowing that the AIS represents the final locus of synaptic interaction and, therefore, is an ideal target for regulating AP initiation, AIS defects may, in turn, alter the shape of the AP. However, here, can we correlate the decrease in AIS length with the modified AP shape observed in our patient? Although only two studies does not find any positive correlation between AIS length and the spike properties (Bonnevie et al., 2020; Moubarak et al., 2019), several other studies demonstrated a clear link between these two parameters in different cell types (Gulledge and Bravo, 2016; Jorgensen et al., 2020; Kaphzan et al., 2011; Kuba et al., 2010). Indeed, Kuba et al. (2010) showed that auditory deprivation increased AIS length in an avian brainstem auditory neuron resulting in a bigger and shorter AP in amplitude and duration, respectively. Also, in hippocampal pyramidal neurons from a mouse model of Angelman syndrome, Kaphzan et al. (2011) demonstrate that neurons from mutant mice have longer AIS resulting in increased AP amplitude, and that AnKG and Nav1.6 are upregulated (Kaphzan et al., 2011). Interestingly, in both studies (Kaphzan et al., 2011; Kuba et al., 2010), increased AIS length correlates with larger AP amplitude and shorter AP duration, resulting in membrane hyperexcitability, while we observe the exact opposite situation: decreased AP amplitude, longer AP duration, shorter AIS length and no hyperexcitability, as exemplified by the fact that the firing gain does not tend towards an hyper-excitable state in our patient's hiPSC-MNs. In the G127X SOD1 Mouse Model of ALS, studies performed in mice before (Bonnevie et al., 2020) and after (Jorgensen et al., 2020) the onset of the disease show that plastic changes in the AIS occur around symptom onset. Knowing that changes in excitability depends more on the AIS location rather than its length (Kuba, 2012; Yamada and Kuba, 2016),

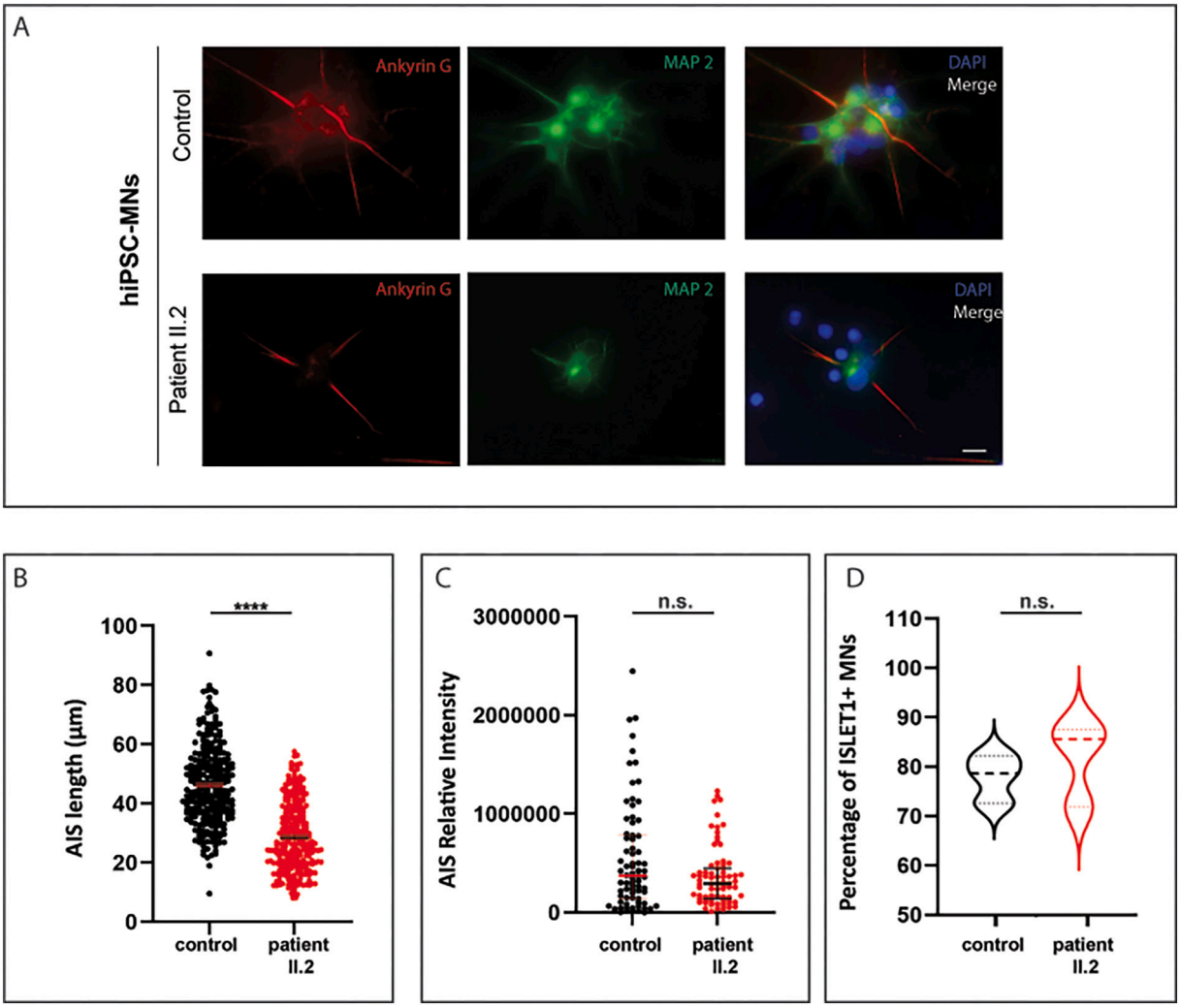

Fig. 6. Shorter AIS in hiPSC-MNs from patient with *VRK1* mutations.
A. Immunolabeling of Ankyrin G and MAP2 in hiPSC-MNs from patient II.2 as compared to control's hiPSC- MNs. **B**. Measure of the AIS length in hiPSC-MNs from patient II.2 as compared to control. AIS length was defined by the length of the AnkyrinG+ segment. Measured AIS length was 46.1 µm and 28.5 µm in control and patient II.2 respectively (average of three independent experiments), showing a decrease of 38% in length in patient's hiPSC-MNs. Measures were performed on 280 hiPSC-MNs counted from three independent experiments. Statistical significance was evaluated by Mann–Whitney test, $*P < 0.1$, $**P < 0.01$, $***P < 0.001$. Data are represented as dot plot graphs with mean ± SEM. **C**. Quantification of AIS intensity by measuring relative intensity of a specified area, using ImageJ software. Data were recorded, for each individual, on 75 AIS segments from three independent experiments. We did not observe any significant differences between patient II.2 and control. Statistical significance was evaluated by a Mann–Whitney test: n.s: not significant. Data are represented as dot plot graphs with median, first and third quartiles. **D**. Percentage of mature hiPSC-MNs at the end of the differentiation protocol (DIV30) was evaluated by counting ISLET1 positive cells, in at least 2000 cells from three independent experiments (2007 cells for control and 2264 cells for patient II.2). These experiments are the same ones used in A–C. Statistical significance was evaluated by unpaired *t*-test, n.s: not significant. Data are represented as violin plots, with median, first and third quartiles.

the specific alteration of the AP with no significant firing defects observed here in patients' MNs might be explained by a change specifically in the length of the AIS, but with preserved distance to soma. Unfortunately, we have not been able to measure this distance due to the fact that hiPSC-MNs differentiate from embryoid bodies, and that soma are therefore not isolated, making it difficult to identify precisely the exit point from the soma.

All together our results demonstrate that Motor Neurons from patients with VRK1-related motor neuron diseases display a modification in the shape of the AP and a depolarized AP threshold with no alteration of the proportion of firing patterns. Many work remains to be done in order to understand which pathophysiological mechanisms lead to these alterations of the AP shape and the AIS, in particular if there is a role of Nav1.6, the link with the loss of Cajal Bodies in patients' MNs (El-Bazzal et al., 2019), and finally, how the structural neurite defects previously described by us in the patients' MNs (El-Bazzal et al., 2019) are related to the AIS anomalies?

5. Conclusion

This study demonstrates that hiPSC-derived motor neurons can recapitulate key disease-related features and constitute an excellent model to study the pathophysiological mechanisms leading to the diseases due to mutations in *VRK1*. Our study places this group of hereditary diseases affecting lower and upper motor neurons, in the expanding group of diseases presenting alterations of AIS components, such as epilepsy, neurodegenerative and neuroinflammatory diseases and psychiatric disorders (Leterrier, 2018). Our findings open new avenues for a better understanding, and perspectives therapeutics, not only for VRK1-related motor neuron diseases, but also for Amyotrophic Lateral Sclerosis and Spinal Muscular Atrophy, the latter sharing cellular defects with the disease affecting our patients.

Author contributions

R.B performed the electrophysiological experiments, analyzed the data, interpreted the results, and wrote the manuscript.

K.R. designed the study, performed cell culture and immunolabeling experiments, analyzed the data and contributed to the writing of the manuscript.

V.D. and F.B. designed the study, analyzed the data, interpreted the results and wrote the manuscript.

P.Q. performed cell culture and immunolabeling, and contributed to the interpretation of the results and edition of the manuscript.

N·D-S performed cell culture.

L.E-B. contributed to the analysis and interpretation of the results and writing of the manuscript.

A.M. and R.B. contributed with materials and edited the manuscript.

N.B.M, M.B. contributed to the interpretation of the results and edited the manuscript.

Supplementary data to this article can be found online at https://doi.org/10.1016/j.nbd.2021.105609.

Declaration of Competing Interest

We declare no conflicts of interest.

Acknowledgments

We thank MaSC, the Cell Reprogramming and Differentiation Facility at U 1251/Marseille Medical Genetics (Marseille, France) for providing the control hiPSC line.

This work was supported by grants from the French associations: 'Association ADN' and the French Association against Myopathies (Association Française contre les Myopathies', Grant # TRIM-RD) and the Lebanese National Council for Scientific Research (CNRS, Grant #S/1257). This work has also been supported by a PRESTIGE programme (PRESTIGE-2017-1-0006, PCOFUND-GA-2013-609102).

References

Bonnevie, V.S., Dimintiyanova, K.P., Hedegaard, A., Lehnhoff, J., Grondahl, L., Moldovan, M., Meehan, C.F., 2020. Shorter axon initial segments do not cause repetitive firing impairments in the adult presymptomatic G127X SOD-1 amyotrophic lateral sclerosis mouse. Sci. Rep. 10, 1280. https://doi.org/10.1038/s41598-019-57314-w.

Bos, R., Harris-Warrick, R.M., Brocard, C., Demianenko, L.E., Manuel, M., Zytnicki, D., Korogod, S.M., Brocard, F., 2018. Kv1.2 channels promote nonlinear spiking Motoneurons for powering up locomotion. Cell Rep. 22, 3315–3327. https://doi.org/10.1016/j.celrep.2018.02.093.

Bucchia, M., Merwin, S.J., Re, D.B., Kariya, S., 2018. Limitations and challenges in modeling diseases involving spinal motor neuron degeneration in vitro. Front. Cell. Neurosci. 12, 61. https://doi.org/10.3389/fncel.2018.00061.

Davis-Dusenbery, B.N., Williams, L.A., Klim, J.R., Eggan, K., 2014. How to make spinal motor neurons. Development 141, 491–501. https://doi.org/10.1242/dev.097410.

Devlin, A.C., Burr, K., Borooah, S., Foster, J.D., Cleary, E.M., Geti, I., Vallier, L., Shaw, C. E., Chandran, S., Miles, G.B., 2015. Human iPSC-derived motoneurons harbouring TARDBP or C9ORF72 ALS mutations are dysfunctional despite maintaining viability. Nat. Commun. 6, 5999. https://doi.org/10.1038/ncomms6999.

Durand, J., Filipchuk, A., Pambo-Pambo, A., Amendola, J., Borisovna Kulagina, I., Gueritaud, J.P., 2015. Developing electrical properties of postnatal mouse lumbar motoneurons. Front. Cell. Neurosci. 9, 349. https://doi.org/10.3389/fncel.2015.00349.

El-Bazzal, L., Rihan, K., Bernard-Marissal, N., Castro, C., Chouery-Khoury, E., Desvignes, J.P., Atkinson, A., Bertaux, K., Koussa, S., Levy, N., et al., 2019. Loss of Cajal bodies in motor neurons from patients with novel mutations in VRK1. Hum. Mol. Genet. 28, 2378–2394. https://doi.org/10.1093/hmg/ddz060.

Filipchuk, A., Pambo-Pambo, A., Gaudel, F., Liabeuf, S., Brocard, C., Patrick Gueritaud, J., Durand, J., 2021. Early hypoexcitability in a subgroup of spinal motoneurons in superoxide dismutase 1 transgenic mice, a model of amyotrophic lateral sclerosis. Neuroscience. https://doi.org/10.1016/j.neuroscience.2021.01.039.

Gao, B.X., Ziskind-Conhaim, L., 1998. Development of ionic currents underlying changes in action potential waveforms in rat spinal motoneurons. J. Neurophysiol. 80, 3047–3061. https://doi.org/10.1152/jn.1998.80.6.3047.

Gonzaga-Jauregui, C., Lotze, T., Jamal, L., Penney, S., Campbell, I.M., Pehlivan, D., Hunter, J.V., Woodbury, S.L., Raymond, G., Adesina, A.M., et al., 2013. Mutations in VRK1 associated with complex motor and sensory axonal neuropathy plus microcephaly. JAMA Neurol. 70, 1491–1498. https://doi.org/10.1001/jamaneurol.2013.4598 1754326 [pii].

Gulledge, A.T., Bravo, J.J., 2016. Neuron morphology influences axon initial segment plasticity. eNeuro 3. https://doi.org/10.1523/ENEURO.0085-15.2016.

Hadzipasic, M., Tahvildari, B., Nagy, M., Bian, M., Horwich, A.L., McCormick, D.A., 2014. Selective degeneration of a physiological subtype of spinal motor neuron in mice with SOD1-linked ALS. Proc. Natl. Acad. Sci. U. S. A. 111, 16883–16888. https://doi.org/10.1073/pnas.1419497111.

Jenkins, S.M., Bennett, V., 2001. Ankyrin-G coordinates assembly of the spectrin-based membrane skeleton, voltage-gated sodium channels, and L1 CAMs at Purkinje neuron initial segments. J. Cell Biol. 155, 739–746. https://doi.org/10.1083/jcb.200109026.

Jorgensen, H.S., Jensen, D.B., Dimintiyanova, K.P., Bonnevie, V.S., Hedegaard, A., Lehnhoff, J., Moldovan, M., Grondahl, L., Meehan, C.F., 2020. Increased axon initial segment length results in increased Na(+) currents in spinal Motoneurones at symptom onset in the G127X SOD1 mouse model of amyotrophic lateral sclerosis. Neuroscience. https://doi.org/10.1016/j.neuroscience.2020.11.016.

Kaphzan, H., Buffington, S.A., Jung, J.I., Rasband, M.N., Klann, E., 2011. Alterations in intrinsic membrane properties and the axon initial segment in a mouse model of Angelman syndrome. J. Neurosci. 31, 17637–17648. https://doi.org/10.1523/JNEUROSCI.4162-11.2011.

Kuba, H., 2012. Structural tuning and plasticity of the axon initial segment in auditory neurons. J. Physiol. 590, 5571–5579. https://doi.org/10.1113/jphysiol.2012.237305.

Kuba, H., Oichi, Y., Ohmori, H., 2010. Presynaptic activity regulates Na(+) channel distribution at the axon initial segment. Nature 465, 1075–1078. https://doi.org/10.1038/nature09087.

Lafarga, M., Tapia, O., Romero, A.M., Berciano, M.T., 2017. Cajal bodies in neurons. RNA Biol. 14, 712–725. https://doi.org/10.1080/15476286.2016.1231360.

Leterrier, C., 2018. The axon initial segment: an updated viewpoint. J. Neurosci. 38, 2135–2145. https://doi.org/10.1523/JNEUROSCI.1922-17.2018.

Liu, H., Lu, J., Chen, H., Du, Z., Li, X.J., Zhang, S.C., 2015. Spinal muscular atrophy patient-derived motor neurons exhibit hyperexcitability. Sci. Rep. 5, 12189. https://doi.org/10.1038/srep12189.

Lopez-Borges, S., Lazo, P.A., 2000. The human vaccinia-related kinase 1 (VRK1) phosphorylates threonine-18 within the mdm-2 binding site of the p53 tumour suppressor protein. Oncogene 19, 3656–3664. https://doi.org/10.1038/sj.onc.1203709.

Maffioletti, S.M., Sarcar, S., Henderson, A.B.H., Mannhardt, I., Pinton, L., Moyle, L.A., Steele-Stallard, H., Cappellari, O., Wells, K.E., Ferrari, G., et al., 2018. Three-dimensional human iPSC-derived artificial skeletal muscles model muscular dystrophies and enable multilineage tissue engineering. Cell Rep. 23, 899–908. https://doi.org/10.1016/j.celrep.2018.03.091.

Manuel, M., Zytnicki, D., 2019. Molecular and electrophysiological properties of mouse motoneuron and motor unit subtypes. Curr. Opin. Physiol. 8, 23–29. https://doi.org/10.1016/j.cophys.2018.11.008.

Martinez-Silva, M.L., Imhoff-Manuel, R.D., Sharma, A., Heckman, C.J., Shneider, N.A., Roselli, F., Zytnicki, D., Manuel, M., 2018. Hypoexcitability precedes denervation in the large fast-contracting motor units in two unrelated mouse models of ALS. eLife 7. https://doi.org/10.7554/eLife.30955.

Maury, Y., Come, J., Piskorowski, R.A., Salah-Mohellibi, N., Chevaleyre, V., Peschanski, M., Martinat, C., Nedelec, S., 2015. Combinatorial analysis of developmental cues efficiently converts human pluripotent stem cells into multiple neuronal subtypes. Nat. Biotechnol. 33, 89–96. https://doi.org/10.1038/nbt.3049.

Mazaleyrat, K., Badja, C., Broucqsault, N., Chevalier, R., Laberthonniere, C., Dion, C., Baldasseroni, L., El-Yazidi, C., Thomas, M., Bachelier, R., et al., 2020. Multilineage differentiation for formation of innervated skeletal muscle fibers from healthy and diseased human pluripotent stem cells. Cells 9. https://doi.org/10.3390/cells9061531.

Moubarak, E., Engel, D., Dufour, M.A., Tapia, M., Tell, F., Goaillard, J.M., 2019. Robustness to axon initial segment variation is explained by Somatodendritic excitability in rat Substantia Nigra dopaminergic neurons. J. Neurosci. 39, 5044–5063. https://doi.org/10.1523/JNEUROSCI.2781-18.2019.

Nguyen, T.P., Biliciler, S., Wiszniewski, W., Sheikh, K., 2015. Expanding phenotype of VRK1 mutations in motor neuron disease. J. Clin. Neuromuscul. Dis. 17, 69–71. https://doi.org/10.1097/CND.0000000000000960.

Nichols, R.J., Traktman, P., 2004. Characterization of three paralogous members of the mammalian vaccinia related kinase family. J. Biol. Chem. 279, 7934–7946. https://doi.org/10.1074/jbc.M310813200.

Renbaum, P., Kellerman, E., Jaron, R., Geiger, D., Segel, R., Lee, M., King, M.C., Levy-Lahad, E., 2009. Spinal muscular atrophy with pontocerebellar hypoplasia is caused by a mutation in the VRK1 gene. Am. J. Hum. Genet. 85, 281–289. https://doi.org/10.1016/j.ajhg.2009.07.006.

Sances, S., Bruijn, L.I., Chandran, S., Eggan, K., Ho, R., Klim, J.R., Livesey, M.R., Lowry, E., Macklis, J.D., Rushton, D., et al., 2016. Modeling ALS with motor neurons derived from human induced pluripotent stem cells. Nat. Neurosci. 19, 542–553. https://doi.org/10.1038/nn.4273.

Sanz-Garcia, M., Vazquez-Cedeira, M., Kellerman, E., Renbaum, P., Levy-Lahad, E., Lazo, P.A., 2011. Substrate profiling of human vaccinia-related kinases identifies coilin, a Cajal body nuclear protein, as a phosphorylation target with neurological implications. J. Proteome 75, 548–560. https://doi.org/10.1016/j.jprot.2011.08.019.

Saporta, M.A., Grskovic, M., Dimos, J.T., 2011. Induced pluripotent stem cells in the study of neurological diseases. Stem Cell Res Ther 2, 37. https://doi.org/10.1186/scrt78.

Saporta, M.A., Dang, V., Volfson, D., Zou, B., Xie, X.S., Adebola, A., Liem, R.K., Shy, M., Dimos, J.T., 2015. Axonal Charcot-Marie-tooth disease patient-derived motor neurons demonstrate disease-specific phenotypes including abnormal electrophysiological properties. Exp. Neurol. 263, 190–199. https://doi.org/10.1016/j.expneurol.2014.10.005.

Sareen, D., O'Rourke, J.G., Meera, P., Muhammad, A.K., Grant, S., Simpkinson, M., Bell, S., Carmona, S., Ornelas, L., Sahabian, A., et al., 2013. Targeting RNA foci in iPSC-derived motor neurons from ALS patients with a C9ORF72 repeat expansion. Sci. Transl. Med. 5, 208ra149. https://doi.org/10.1126/scitranslmed.3007529.

Smith, C.C., Brownstone, R.M., 2020. Spinal motoneuron firing properties mature from rostral to caudal during postnatal development of the mouse. J. Physiol. 598, 5467–5485. https://doi.org/10.1113/JP280274.

Takahashi, K., Yamanaka, S., 2006. Induction of pluripotent stem cells from mouse embryonic and adult fibroblast cultures by defined factors. Cell 126, 663–676. https://doi.org/10.1016/j.cell.2006.07.024.

Takahashi, K., Tanabe, K., Ohnuki, M., Narita, M., Ichisaka, T., Tomoda, K., Yamanaka, S., 2007. Induction of pluripotent stem cells from adult human fibroblasts by defined factors. Cell 131, 861–872. https://doi.org/10.1016/j.cell.2007.11.019.

Tapia, O., Bengoechea, R., Palanca, A., Arteaga, R., Val-Bernal, J.F., Tizzano, E.F., Berciano, M.T., Lafarga, M., 2012. Reorganization of Cajal bodies and nucleolar targeting of coilin in motor neurons of type I spinal muscular atrophy. Histochem. Cell Biol. 137, 657–667. https://doi.org/10.1007/s00418-012-0921-8.

Tazerart, S., Viemari, J.C., Darbon, P., Vinay, L., Brocard, F., 2007. Contribution of persistent sodium current to locomotor pattern generation in neonatal rats. J. Neurophysiol. 98, 613–628. https://doi.org/10.1152/jn.00316.2007.

Toli, D., Buttigieg, D., Blanchard, S., Lemonnier, T., Lamotte d'Incamps, B., Bellouze, S., Baillat, G., Bohl, D., Haase, G., 2015. Modeling amyotrophic lateral sclerosis in pure human iPSc-derived motor neurons isolated by a novel FACS double selection technique. Neurobiol. Dis. 82, 269–280. https://doi.org/10.1016/j.nbd.2015.06.011.

Valbuena, A., Lopez-Sanchez, I., Vega, F.M., Sevilla, A., Sanz-Garcia, M., Blanco, S., Lazo, P.A., 2007. Identification of a dominant epitope in human vaccinia-related kinase 1 (VRK1) and detection of different intracellular subpopulations. Arch. Biochem. Biophys. 465, 219–226. https://doi.org/10.1016/j.abb.2007.06.005.

Valbuena, A., Lopez-Sanchez, I., Lazo, P.A., 2008. Human VRK1 is an early response gene and its loss causes a block in cell cycle progression. PLoS One 3, e1642. https://doi.org/10.1371/journal.pone.0001642.

Valbuena, A., Sanz-Garcia, M., Lopez-Sanchez, I., Vega, F.M., Lazo, P.A., 2011. Roles of VRK1 as a new player in the control of biological processes required for cell division. Cell. Signal. 23, 1267–1272. https://doi.org/10.1016/j.cellsig.2011.04.002.

Vinay, L., Brocard, F., Clarac, F., 2000. Differential maturation of motoneurons innervating ankle flexor and extensor muscles in the neonatal rat. Eur. J. Neurosci. 12, 4562–4566. https://doi.org/10.1046/j.0953-816x.2000.01321.x.

Wainger, B.J., Kiskinis, E., Mellin, C., Wiskow, O., Han, S.S., Sandoe, J., Perez, N.P., Williams, L.A., Lee, S., Boulting, G., et al., 2014. Intrinsic membrane hyperexcitability of amyotrophic lateral sclerosis patient-derived motor neurons. Cell Rep. 7, 1–11. https://doi.org/10.1016/j.celrep.2014.03.019.

Yaffe, D., Saxel, O., 1977. Serial passaging and differentiation of myogenic cells isolated from dystrophic mouse muscle. Nature 270, 725–727. https://doi.org/10.1038/270725a0.

Yamada, R., Kuba, H., 2016. Structural and functional plasticity at the axon initial segment. Front. Cell. Neurosci. 10, 250. https://doi.org/10.3389/fncel.2016.00250.

Yoshida, M., Kitaoka, S., Egawa, N., Yamane, M., Ikeda, R., Tsukita, K., Amano, N., Watanabe, A., Morimoto, M., Takahashi, J., et al., 2015. Modeling the early phenotype at the neuromuscular junction of spinal muscular atrophy using patient-derived iPSCs. Stem Cell Rep. 4, 561–568. https://doi.org/10.1016/j.stemcr.2015.02.010.

Zhou, D., Lambert, S., Malen, P.L., Carpenter, S., Boland, L.M., Bennett, V., 1998. AnkyrinG is required for clustering of voltage-gated Na channels at axon initial segments and for normal action potential firing. J. Cell Biol. 143, 1295–1304. https://doi.org/10.1083/jcb.143.5.1295.